Advanced Materials Interfaces

ADVANCED MATERIALS INTERFACES Open Access

www.advmatinterfaces.de

RESEARCH ARTICLE OPEN ACCESS

Layered Nanoporous Platforms for SERS Sensing

Yanqiu Zou[1] | Anastasiia Sapunova[2,3] | Tommaso Giovannini[4] | Chen Wang[5] | Huaizhou Jin[6] | Vincenzo Caligiuri[7] | Sergio Marras[2] | Andrea Schirato[8,9] | Luca Bursi[10] | Alessandro Alabastri[9] | Shukun Weng[2,3] | Ali Douaki[2,11] | German Lanzavecchia[2,11] | Ivan Marri[11] | Roman Krahne[2] | Nicolò Maccaferri[12,13] | Zhenrong Zheng[1] | Shangzhong Jin[5] | Denis Garoli[2,5,11]

[1]State Key Laboratory of Modern Optical Instrumentation, College of Optical Science and Engineering, Zhejiang University, Hangzhou, China | [2]Istituto Italiano di Tecnologia, Genova, Italy | [3]Università degli Studi di Milano-Bicocca, Milano, Italy | [4]Department of Physics, University of Rome Tor Vergata, and INFN, Rome, Italy | [5]College of Optical and Electronic Technology, China Jiliang University, Hangzhou, China | [6]Key Laboratory of Quantum Precision Measurement, College of Physics, Zhejiang University of Technology, Hangzhou, China | [7]Dipartimento Di Fisica, Università della Calabria, Cosenza, Italy | [8]Dipartimento Di Fisica, Politecnico di Milano, Milano, Italy | [9]Department of Physics and Astronomy, Rice University, Houston, Texas, USA | [10]Department of Physical, Computer, and Mathematical Sciences (FIM), Università degli Studi di Modena e Reggio Emilia, and Nanoscience Institute, CNR-NANO, Modena, Italy | [11]Università degli Studi di Modena e Reggio Emilia, Reggio Emilia, Italy | [12]Ultrafast Nanoscience Group, Department of Physics, Umeå University, Umeå, Sweden | [13]Umeå Centre for Microbial Research, Umeå University, Umeå, Sweden

Correspondence: Zhenrong Zheng (zzr@zju.edu.cn) | Shangzhong Jin (Jinsz@cjlu.edu.cn) | Denis Garoli (denis.garoli@unimore.it)

Received: 8 January 2026 | **Revised:** 2 May 2026 | **Accepted:** 10 May 2026

Keywords: copper | gold | nanoporous materials | plasmonics | raman | silver

ABSTRACT

Nanoporous metals have been widely explored as platforms for plasmonic applications due to their high surface area and the strong localized electromagnetic fields they support. These properties can be tuned over a broad energy range by controlling both the metal composition and the morphology of the porous network. Until recently, most studies focused on nanoporous structures composed of a single metal, while the influence of alloyed or multi-metal systems remained largely unexplored. Only in recent years the interest in bimetallic nanoporous systems begun to grow. Combining two or more plasmonic metals provides a powerful strategy to investigate intermetallic interactions, including plasmonic coupling, charge transfer, interfacial band hybridization, and electromagnetic field interactions, as well as thermal and electronic energy transfer depending on the system geometry. Bimetallic nanoporous platforms are also highly relevant for biomolecular sensing, particularly in Surface-Enhanced Raman Scattering (SERS). In this work, we present the first detailed study of bimetallic nanoporous platforms fabricated via a dry-synthesis approach, enabling simple and controllable fabrication of layered structures combining metals such as Au, Ag, and Cu. Experimental results, supported by numerical simulations, demonstrate that these layered systems allow electromagnetic field localization at distinct energies, with synergistic effects arising from different bimetallic configurations.

1 | Introduction

Over the last decades, research on nanoporous metals (NPMs) has grown steadily, driven by their broad range of applications in sensing [1, 2], catalysys [3–5], photonics [6–9] and biomedicine [10]. The main characteristic of NPMs is their high surface-to-volume ratio that, combined with unique chemical reactivity and mass transport properties, makes this family of nanostructured materials highly interesting for advanced research. NPMs can be prepared following different strategies such as

Yanqiu Zou and Anastasiia Sapunova contributed equally to this work.

template-assisted physical vapor deposition, electrochemical processes, and chemical dealloying [11]. The latter is probably the most used method to prepare NPMs through selective dissolution of the more chemically active component from precursor alloys. Dealloying methods have been applied to prepare NPMs as gold [12, 13], copper [14, 15], silver [16, 17] and aluminum [18–20]. A specific aspect of dealloying is the presence of residual less noble metal at the end of the process. This effect is difficult to avoid and leads to resulting nanoporous structures with varying alloy compositions [21, 22]. Interestingly, this residual "contamination" in the final porous film, long considered as a limitation in the preparation of pure porous structures, has recently been shown to enhance plasmonic properties of nanoporous gold containing residual amount of the less noble metal due to modulation of its permittivity by the alloying components [23, 24]. The combination of two or more metals in alloys is a strategy to provide a way to tune the electronic state through charge transfer between the metals, making it possible to alter the chemical interaction between molecules and the surface of the alloy. In particular, the adsorption behavior of molecules having either high electronegativity (e.g., oxygen and halogens), strong polarity (e.g., carbonyl and nitro groups), partial charge (e.g., carboxylate and hydride-like hydrogen), or high electron density (e.g., alkenes and arenes) is affected by the alloy composition. For instance, palladium-silver alloy promoted the adsorption of negatively charged molecules (carboxylate intermediate) due to the high electronegativity of silver. The alteration of the electronic state by alloying on the molecular detection capability has been recently studied by La et al. [24]. In particular, a SERS enhancement of up to six orders of magnitude for nanoporous gold containing silver was observed and attributed to the narrowing of the electronic structure and its alignment close to the Fermi level. These results suggest that the electronic state modulation of the metal structure can affect molecule-surface interactions. It is also worth noting that bimetallic systems have been reported not only as alloys but also as heterostructures, where the combination of two metals is exploited to tune the optical response, especially in SERS experiments [25–30].

In contrast to previous reports on bimetallic SERS platforms, we investigate multi-metallic nanoporous systems composed of Au, Ag, and Cu, fabricated via a dry-synthesis method [31–33]. The resulting architectures consist of well-defined, spatially separated layers formed by multiple thin nanoporous metal (NPM) films, each comprising a single, highly pure porous metal. This configuration is enabled by the unique capabilities of the fabrication method, which allows for the sequential deposition of nanoporous metals, as previously demonstrated. [32, 33] To the best of our knowledge, this work represents the first realization of perfectly stacked nanoporous metal layers. These structures constitute a versatile platform for elucidating the role of multimetallic architectures in SERS, enabling systematic investigation of enhancement mechanisms at different excitation wavelengths across the visible spectrum. Experimental results, supported by numerical simulations, provide insight into the plasmonic behavior of these novel nanoporous layered systems.

2 | Materials and Methods

2.1 | Samples Fabrication

The samples preparation is based on the original methods proposed by Kwon et al. [31]. In brief, poly (methyl methacrylate) (PMMA) was spin-coated on a Si substrate at 4000 rpm for 2 min. Each metal (>99.99% purity) was subsequently deposited by electron-beam evaporation onto the PMMA thin film at room temperature with an oblique incidence angle of 80°, a deposition rate of 0.1 nm/s, and a target thickness of about 12 nm. The deposited Au film was plasma treated in O_2 at a power of 200 W until the entire PMMA layer was removed. In the case of Ag and Cu films, in order to avoid fast oxidation, the plasma treatment was performed in N_2 at 200 W until the PMMA layer was completely removed (as previously demonstrated, this ensures that the oxidation is kept to a very low level [32]). The bi-layer structures were obtained by repeating the preparation using the first porous layer as substrate for the deposition of the second porous layer on top. Similarly, the tri-layer structures shown in the Supporting Information were fabricated by sequentially depositing the third porous layer onto the pre-formed bi-layer substrate.

2.2 | Spectroscopic Measurements

Raman spectroscopy measurements were performed using a HORIBA LabRAM HR Evolution Raman spectrometer (HORIBA Jobin Yvon, Kyoto, Japan) with a 50X long-focal-length objective (NA = 0.75), a 100μm-hole aperture, and a 600 gr/mm grating. SERS spectra of Rhodamine 6G (R6G) were acquired under different conditions to characterize system performance: 0.1 μM R6G with laser power attenuated to 10% at 532 nm excitation; 1 μM R6G with 5% laser power at 633 nm; and 100 μM R6G with full laser power (no attenuation) at 785 nm. For each substrate, a Raman map was collected over a 20 × 20 μm^2 area with a step size of 5 μm, resulting in 25 individual spectra. Each spectrum was acquired with an integration time of 10 s. The final spectrum of R6G for each substrate was generated by averaging these 25 spectra after pre-processing. Spectra of the protein ADAMTS3 were obtained by averaging five randomly collected spectra, using a 5% ND filter and 60s acquisition time for both 532 and 633 nm excitations. For 785 nm excitation, a 100% ND filter (no attenuation) and 120s acquisition time were used.

2.3 | X-Ray Diffraction (XRD)

X-ray diffraction analysis was carried out on a Malvern-PANalytical third generation Empyrean x-ray powder diffractometer. The instrument was equipped with a 1.8 kW CuKα ceramic x-ray tube operating at 45 kV and 40 mA, iCore and dCore automated PreFIX optical modules, motorized Eulerian Cradle (chi, phi,x,y and z movements) and solid-state hybrid pixel PIXcel3D detector acquiring in 1D mode.

XRD patterns of the films deposited on (100)-oriented silicon wafers were collected in air at room temperature over a 2θ range of 35°–54°, using a step size of 0.053°.

2.4 | Data Analysis

The raw spectra were baseline-corrected and smoothed using HORIBA LabSpec6 software. Subsequently, all data averaging, normalization, spectral deconvolution, peak fitting, and graphical plotting were performed using OriginPro 2025b.

2.5 | Numerical Modelling

To explore the plasmonic properties of layered NPMs, we performed a numerical investigation of the electromagnetic response using a finite element method (FEM) commercial software, employing COMSOL Multiphysics. In particular, following a procedure reported in detail in our recently reported works [33, 34], nanometric pores and irregularities of NPMs have been numerically reproduced from scanning electron microscopy (SEM) images of the experimental samples. However, continuum modeling, such as FEM, might fail in describing the response properties of bimetallic nanostructured materials. Therefore, to validate the FEM procedure, the optical response of NPMs has also been calculated using a fully atomistic approach, named frequency-dependent fluctuating charges and dipoles (ωFQFμ) [35–37]. This method provides a reliable description of noble metal nanoparticles, comparable to ab initio but at significantly lower computational cost, enabling to handle systems composed of thousands of atoms [38, 39]. Remarkably, it can also be applied to bimetallic systems and, in the specific case of Au/Ag nanoparticles, yields results in almost perfect agreement with experiment [40]. For cross-validation of the COMSOL results, we have adopted an idealized picture in which the same porous structure is generated and then considered either as Ag or Au, which are characterized by the same lattice constant (4.08 Å). Such structures were created by introducing randomly generated nanometric pores, thereby generating realistic surface roughness and porosity. In particular, we modeled a $7 \times 7 \times 4$ (nm^3) structure, composed of 6584 atoms, a size unfeasible for ab initio atomistic models (see SI for a graphical representation). The same nanoporous geometry was then used to simulate Ag/Ag, Au/Au, and Au/Ag bilayers, allowing for a direct comparison of their optical response and a detailed analysis of the different compositional effects. All ωFQFμ calculations are performed using the Ag/Au parameters reported in Nicoli et al. [40]., with the open-source plasmonX software [41].

2.6 | Dielectric Permittivity and Ellipsometry

Spectroscopic ellipsometry was employed to determine the dielectric permittivity of nanoporous Ag/Ag, Ag/Au, and Ag/Cu bilayers (ellipsometric data related to Au/Ag and Cu/Cu were reported by Caligiuri et al. [33]. and Tapani et al. [32].). The measurements provided both the real and imaginary components of the dielectric function over the visible range. The experimental data were fitted using a model composed of Lorentzian and Gaussian oscillators to capture the main features of each alloy's optical response. The resulting dielectric permittivities accurately reproduce the experimental ellipsometric parameters Ψ and Δ. Complete fitting details and oscillator parameters are reported in the (Table S1).

3 | Results and Discussion

Figure 1 shows the planar morphologies of the samples used in these experiments (additional micrographs are reported in SI for the three layers systems). The first row (Figure 1a–c) presents the single-metal NPM films, Au, Ag, and Cu, respectively, whereas the remaining micrographs depict the morphologies of the bi-metallic layered films. The single-metal films exhibit a nanoporous structure characterized by fully interconnected ligaments with diameters on the order of a few tens of nanometers. In contrast, the bi-metallic layered films display markedly different morphologies depending on the sample. In all bi-metallic cases (Figure 1d–i), the two metallic layers are clearly distinguishable and appear stacked rather than intermixed. To verify the preparation of not mixed nanoporous layers, XRD analyses (see SI for details) were performed on the prepared samples, showing no peaks associated to mixed phases (such as Au_xAg_y, Au_xCu_y or Ag_xCu_y). This morphological feature is enabled by the dry synthesis process employed. As demonstrated in our previous work [33] the layer-by-layer thin-film deposition combined with plasma treatment allows the formation of well-separated NPM layers. To the best of our knowledge, such a degree of layer separation cannot be achieved using conventional dealloying methods or template-based deposition techniques.

The SEM micrographs were also used to perform a statistical analysis of the size distribution of pores. In most cases, the pore size varies in a wide range of 10–120 nm, while most of them are 40–70 nm. The thickness of the ligaments is 15–50 nm, with an estimated porosity of about 40%–50%. Depending on the configuration of the metals (top and bottom), there are differences in the degree of coarsening of the structure. For example, Au/Ag and Ag/Cu have a finer and more uniform morphology with smaller characteristic pore sizes (30–50 nm) and a narrower distribution. On the contrary, structures such as Cu and Au/Cu exhibit a pronounced enlargement of the structure with an increase in pores to 80–150 nm and a thickening of the ligaments to 40–100 nm. Structures with metal configurations such as Ag/Au, Cu/Au, and Cu/Ag are characterized by a wider pore size distribution (20–130 nm), indicating partial enlargement of the structure.

We subsequently carried out numerical simulations to investigate the electromagnetic response of the porous bilayer system. These simulations provide insight into the electromagnetic (EM) field distributions at the excitation wavelengths employed in the experiments. The nanometric structural features of the layers were directly reconstructed from SEM images of the experimental samples and incorporated into a finite-element-method (FEM) model developed in COMSOL Multiphysics. In particular, top-view SEM micrographs of the Au, Ag, and Cu films were imported into the FEM solver and extruded along the thickness direction to generate the three-dimensional numerical geometries. This approach allowed us to accurately capture the actual material profiles and nanoscale discontinuities of the porous structures.

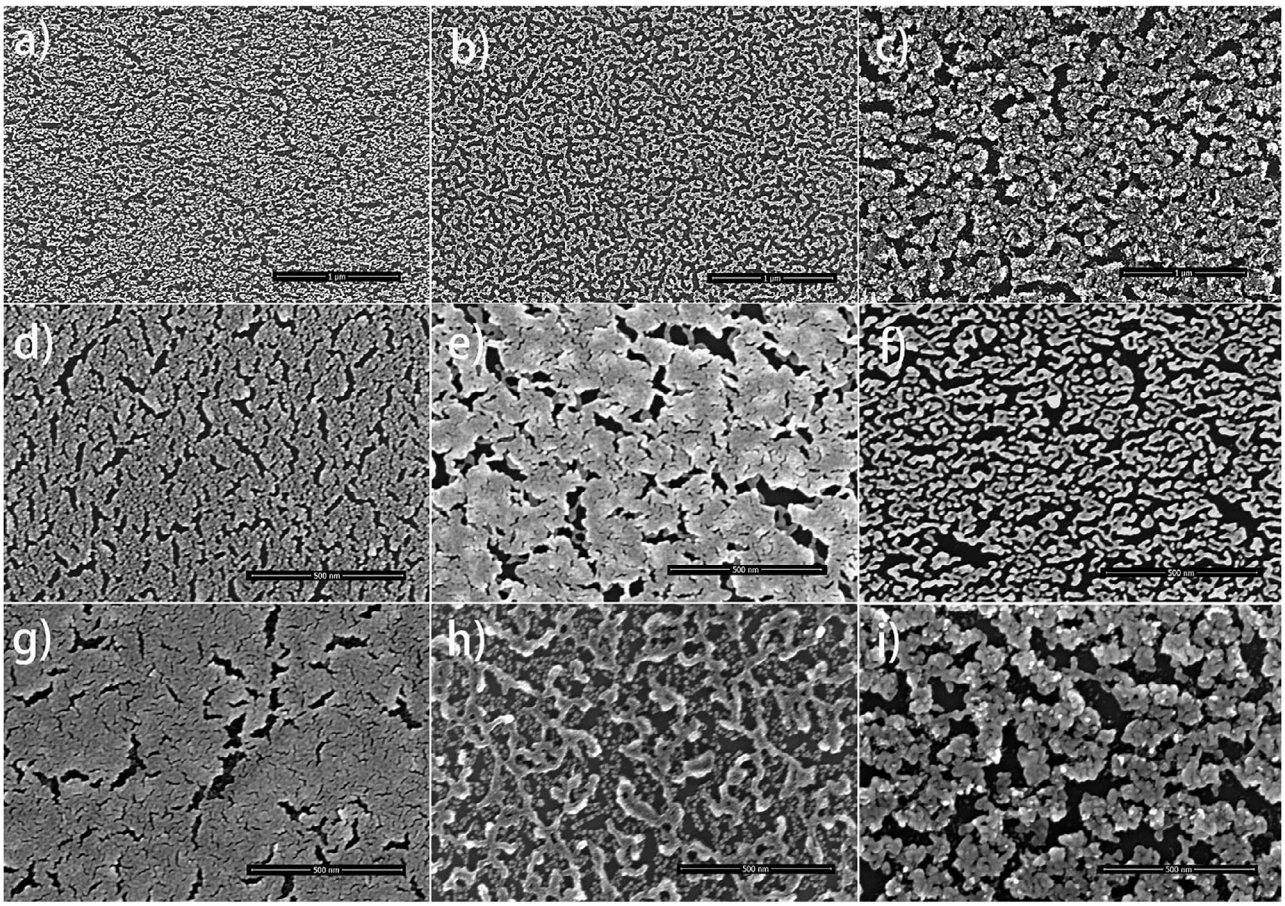

FIGURE 1 | (a–e) SEM micrographs of the investigated samples; porous layers of (a) Au; (b) Ag; (c) Cu; (d) Au/Ag; (e) Ag/Au; (f) Au/Cu; (g) Cu/Au; (h) Ag/Cu; (i) Cu/Ag.

Figures 2–5 present the calculated EM field enhancement distributions along the surfaces of the two porous layers (top and bottom) for the different configurations, evaluated at three excitation wavelengths: 532, 633, and 785 nm.

Figure 2 shows the EM field distributions at wavelengths of 532, 633, and 785 nm for bi-layer nanoporous structures made of a single metal: Cu (a, top), Au (a, middle), and Ag (a, bottom). For the specific case of Au and Ag, the EM distributions are also computed using the fully atomistic ωFQFμ method (Figure 2b). In particular, ωFQFμ provides an accurate description of bimetallic systems, with a level of reliability comparable to ab initio approaches, and it reproduces experimental observations with excellent agreement, also for small gaps characterizing porous systems. This performance stems from its physical grounds and its atomistic formulation. Moreover, its classical nature enables simulations of relatively large systems, although still limited in size compared to fully implicit continuum descriptions such as those provided by FEM.

In this work, we therefore employ model structures for ωFQFμ simulations, aimed at validating FEM as an effective tool for the qualitative rationalization of our experimental results. In all cases, the EM enhancement profiles were evaluated on the surface of the bi-layer structure. The color scale indicates a normalized intensity of the EM field, calculated as the ratio of the electric field in the presence of nanoporous metals to the incident field. All field maps are normalized to the same values, pointing out the regions where the EM field is highly localized. Nevertheless, at the FEM level (Figure 2a), each homometallic sample is characterized by its own geometry and plasmonic properties; therefore, the diagram of the maximum intensities of the EM field is shown for each case (Figure 2c). The strongest enhancement across all studied wavelengths is observed for Ag at 633 nm, whereas Cu shows the weakest response, with almost negligible activity at 532 nm. For Cu and Au, the localized enhanced fields are mainly observed in the pore gaps, whereas in nanoporous Ag, there are a large number of "hot spots" strongly affecting the distribution of the field. Similar results are also obtained at the ωFQFμ level (see Figure 2b) for Ag and Au NPMs. In this case, the electric field shows enhancement distributions depending on the metal and the laser frequency, reflecting a different induced density on the surface. In particular, as for FEM results, the response of Ag NPM is significantly larger than that of Au NPM, and more hot-spots can be observed. Nevertheless, the trends of the maximum electric field enhancements do not correlate exactly with those computed by using FEM (see Figure 2c,d): in fact, in both Ag and Au NPMs, the maximum enhanced field is reported at 785 nm. This can, however, be due to the diverse plasmonic response provided by the two models, and by the small model structure considered in ωFQFμ calculations.

Understanding the optical response of homometallic nanoporous structures at different excitation wavelengths is crucial for a

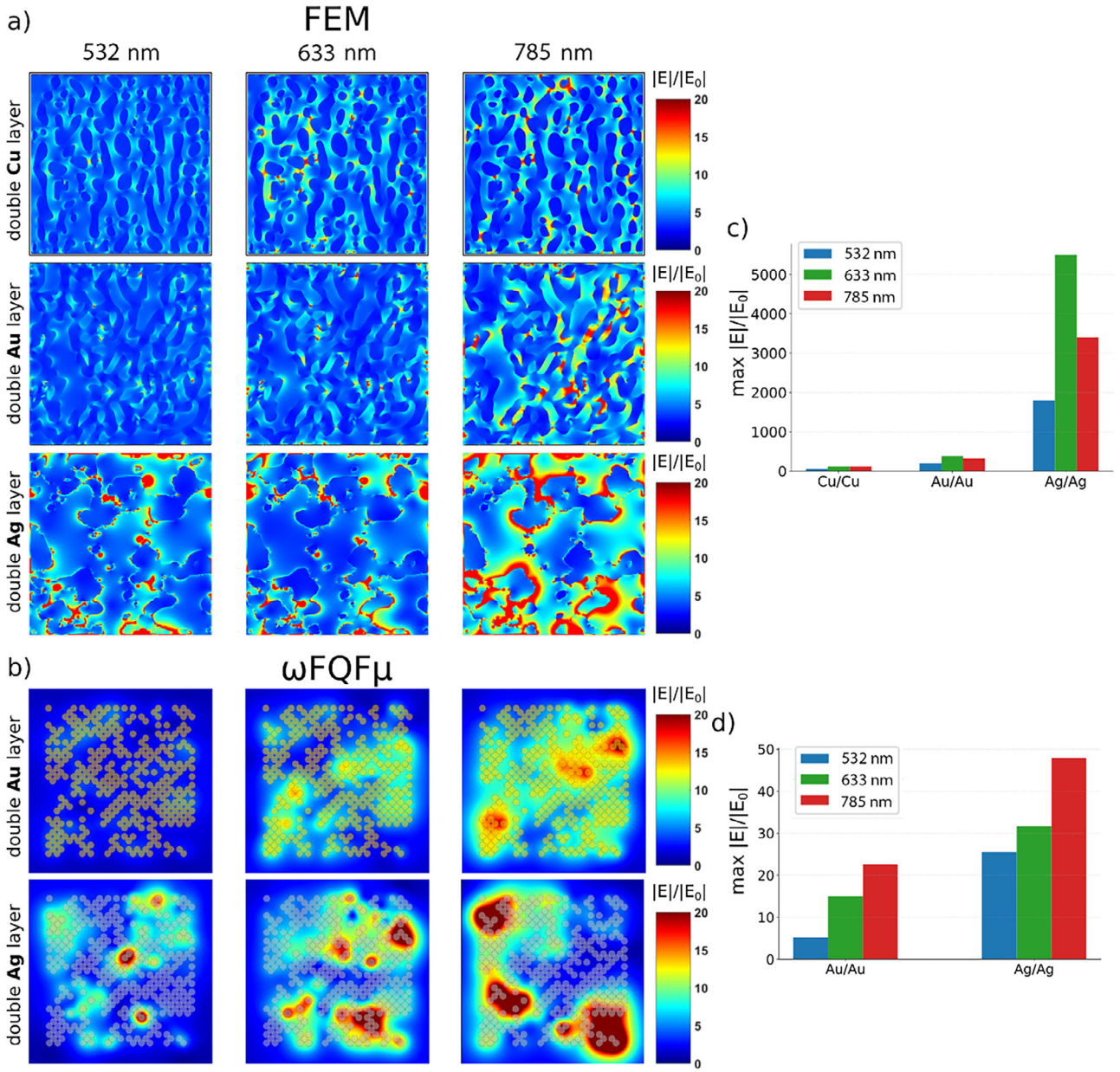

FIGURE 2 | (a,b) EM field enhancement distributions for (a) homometallic nanoporous bilayer structures composed of Cu (top), Au (middle), and Ag (bottom), calculated with FEM at excitation wavelengths of 532, 633, and 785 nm (from left to right); (b) homometallic nanoporous bilayers composed of Au (top) and Ag (bottom), obtained using the ωFQFμ approach at the same excitation wavelengths. All maps are normalized to the same color scale to highlight spatial regions of strongest field enhancement localization. (c,d) Maximum field enhancement values extracted from FEM (c) and ωFQFμ (d) simulations for each structure.

deeper comprehension of the processes occurring across the layers in bi-metallic configurations and for disentangling the individual contribution of each metal. Accordingly, new plasmonic effects emerge in Au/Ag, Ag/Au, Au/Cu, Cu/Au, Ag/Cu, and Cu/Ag NPM systems as a result of interlayer coupling and interactions between the constituent metals. Figure 3 depicts the EM field enhancement distributions for Au/Ag and Ag/Au NPMs (a-b) and field enhancement maxima (c-d) at different wavelengths computed by using FEM (a-c) and at the ωFQFμ level (b-d). At both levels, in the Au/Ag bilayer, the silver layer (Figure 3a), which is placed on top of Au, displays significantly reduced EM field intensity at all studied wavelengths relative to the homometallic Ag layer (Figure 2a,b). Nevertheless, the Ag layer exhibits stronger plasmonic activity, despite the less intense localization of hot spots caused by the electrodynamical interaction between two porous layers consisting of two different plasmonic materials. Interestingly, at the FEM level, illumination of the Ag/Au NPM at 785 nm produces a field enhancement comparable to that at 633 nm (Figure 3c, top), which can likely be associated with the interaction between plasmonic modes of silver and gold. This is also confirmed by the field maps computed at the ωFQFμ level and by the maximum field enhancements, which are similar at all considered frequencies (Figure 3d, top). The same interaction induces a stronger enhancement for Au layer (Figure 3c,d) at 532 nm than in the homometallic layer (Figure 2c,d) and rises with increasing

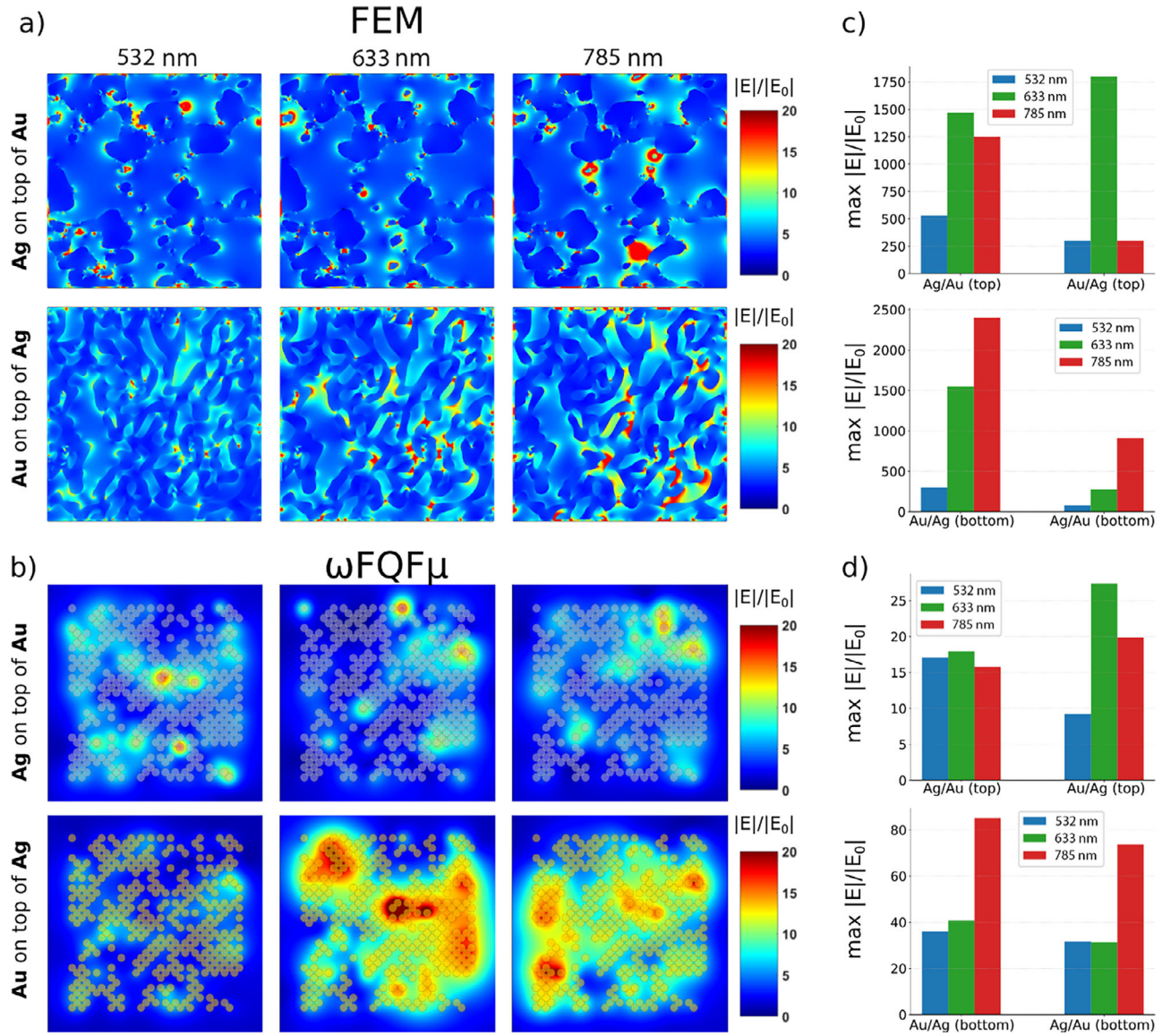

FIGURE 3 | (a,b) The enhanced EM field distribution of Au and Ag layers for Ag/Au (top) and Au/Agu (bottom) NPMs calculated at the FEM (a) and ωFQFμ (b) levels of theory. (c,d) FEM c) and ωFQFμ (d) field enhancement maxima for each structure on top and bottom sides.

wavelength, a trend that is perfectly reproduced qualitatively by both methods.

By contrast, when the Au layer is deposited on Ag (Au/Ag, Figure 3a,b, bottom), the plasmonic response (at the top interface) remains weak at 532 and 785 nm but increases markedly at 633 nm due to interlayer coupling. This notable behavior, consistently reproduced by both numerical approaches (see Figure 3c,d), demonstrates that the stacking order plays a critical role in determining the resonance conditions. Consequently, at 633 nm, silver exhibits a weaker plasmonic response than in the homometallic Ag configuration. Comparing the two heterostructures (Au/Ag and Ag/Au) at 532 nm, the enhancement is stronger when Ag is the top layer, in agreement with silver's superior plasmonic performance in the visible range and its more effective near-field confinement. Furthermore, the wavelength-dependent trends of the enhanced field maxima predicted by the two numerical methods are qualitatively consistent, thereby validating the FEM-based approach used in the subsequent analyses.

Although Au and Cu do not show the strong plasmonic response of Ag (Figure 2), their coupling still produces noteworthy effects. Figure 4 compares the EM field enhancement distributions and maxima for Au/Cu and Cu/Au bilayer configurations. In the case of Cu as upper layer (Figure 4a–c), low plasmonic enhancement of Cu is compensated by coupling with underlying Au, especially at longer wavelengths (785 nm). When Au is on top of Cu (Figure 4g–i), instead, the enhancement is mainly determined by the Au layer itself, while Cu acts as a substrate preventing additional EM field enhancement, possibly because of significant losses in the Cu layer. Interestingly, the field EM enhancement intensities of Cu are mostly the same in combination with Ag (Figure 5). In bimetallic structures Ag/Cu (Figure 5a–f) and Cu/Ag (Figure 5g–l), the EM field enhancement is dominated by Ag, while Cu mainly shows negligible activity, as can be seen from a comparison between the EM field enhancement maxima of these configurations and those of the homometallic structure composed of Ag (Figure 2a, bottom). For Cu located on top of Ag, the lower Ag layer still supports a strong EM field localization,

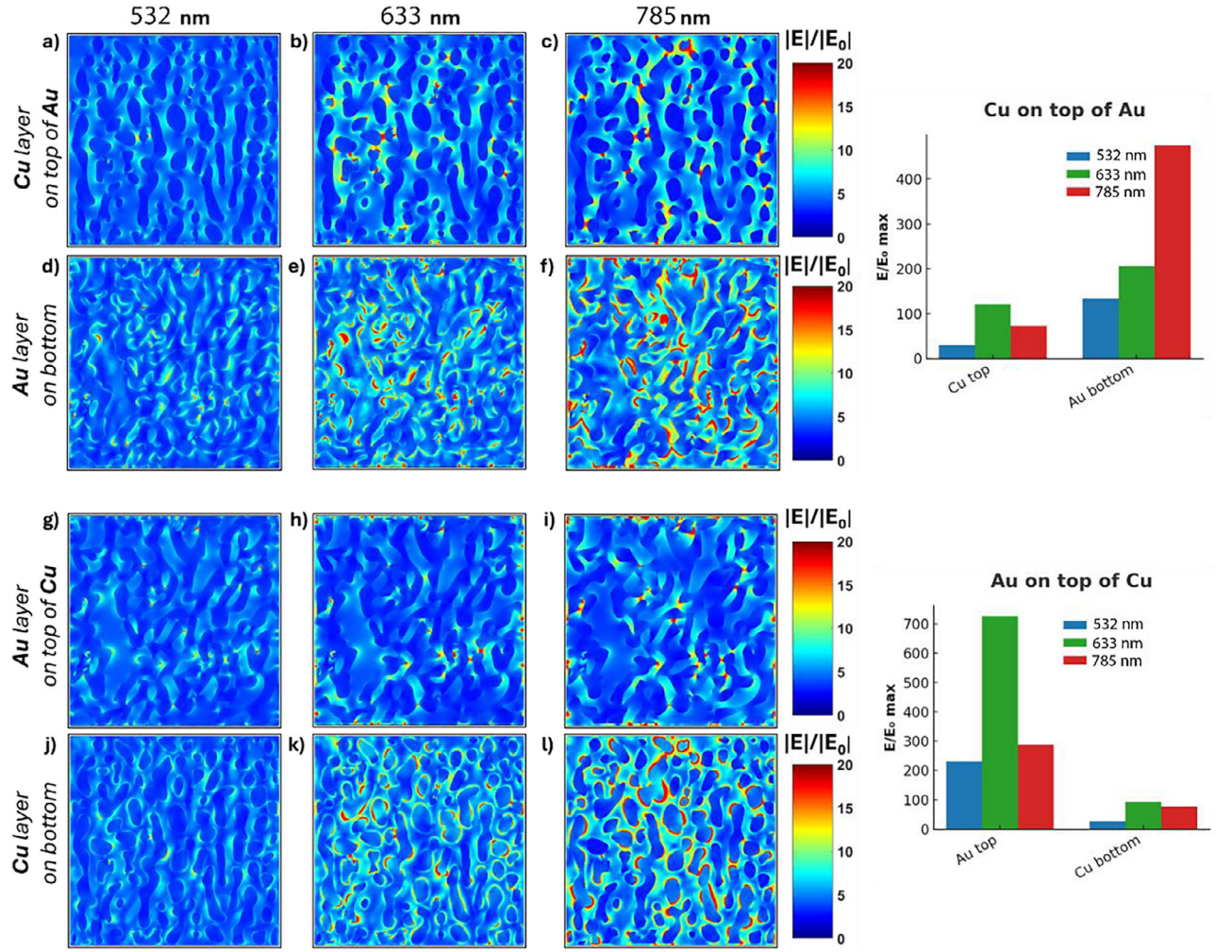

FIGURE 4 | The enhanced EM field distribution of Au and Cu layers for(a–f) Au/Cu and (g–l) Cu/Au NPMs calculated as a ratio of the electric field in the presence of nanoporous metals to the incident field for different wavelengths.

though slightly reduced due to copper-induced losses. In contrast, when Ag is deposited on top of Cu, the EM field enhancement is intensively concentrated in the upper Ag layer, but the overall response, as mentioned earlier, is reduced compared to Ag alone due to the lossy Cu layer. These results confirm that the stacking order determines whether the Cu layer suppresses the Ag layer's resonances or favors the interlayer EM interactions.

These conclusions are also supported by ellipsometric investigations that allowed us to retrieve the dielectric permittivities of the bi-metallic combinations (see Supporting Information). In particular, homometallic bi-layer Ag/Ag exhibits a pronounced metallic response with a negative real permittivity throughout the visible range, confirming its validity as a plasmonic material and efficient field confinement. Ag/Au shows broader dispersion and larger optical losses, reflecting its intrinsically damped plasmonic character. Conversely, Ag/Cu displays a largely suppressed plasmonic response, with the real part of ε only weakly negative and significant absorption across the visible spectrum.

The numerical results provide a framework for understanding and analyzing data during SERS experiments on the investigated bi-metallic NPMs. As predicted by our calculations, the efficiency of EM field enhancement and distribution in bi-layer systems is determined not only by the type of metal, but also by the order of the layers and the coupling efficiency between them. At the excitation energies explored here, in Au—Ag systems, silver dominates in terms of enhancement intensity, whereas the enhancement of gold is explained by the coupling of plasmonic modes. In the case of Ag—Cu, the interlayer coupling is weak, and the enhancement is determined mainly by silver. For Au—Cu, gold dominates in intensity. Additionally, the observed enhancement is still higher than in homometallic structures but remains significantly lower compared to configurations containing Ag.

Guided by the enhanced EM field distributions and coupling interactions between layers predicted above, the SERS performance of these NPMs was evaluated under conditions closely matching those used in the simulations (Figure 6). Figure 6a–c compares the averaged SERS spectra of R6G acquired from a series of NPM configurations with different bilayer stacking sequences (e.g., Au/Cu, Ag/Au), enabling a systematic assessment of their relative enhancement efficiencies. The intensities of five characteristic R6G Raman bands at 620, 1280, 1360, 1509, and 1649 cm^{-1} (identified by asterisks in Figure 6a–c) for the three highest-performing NPM

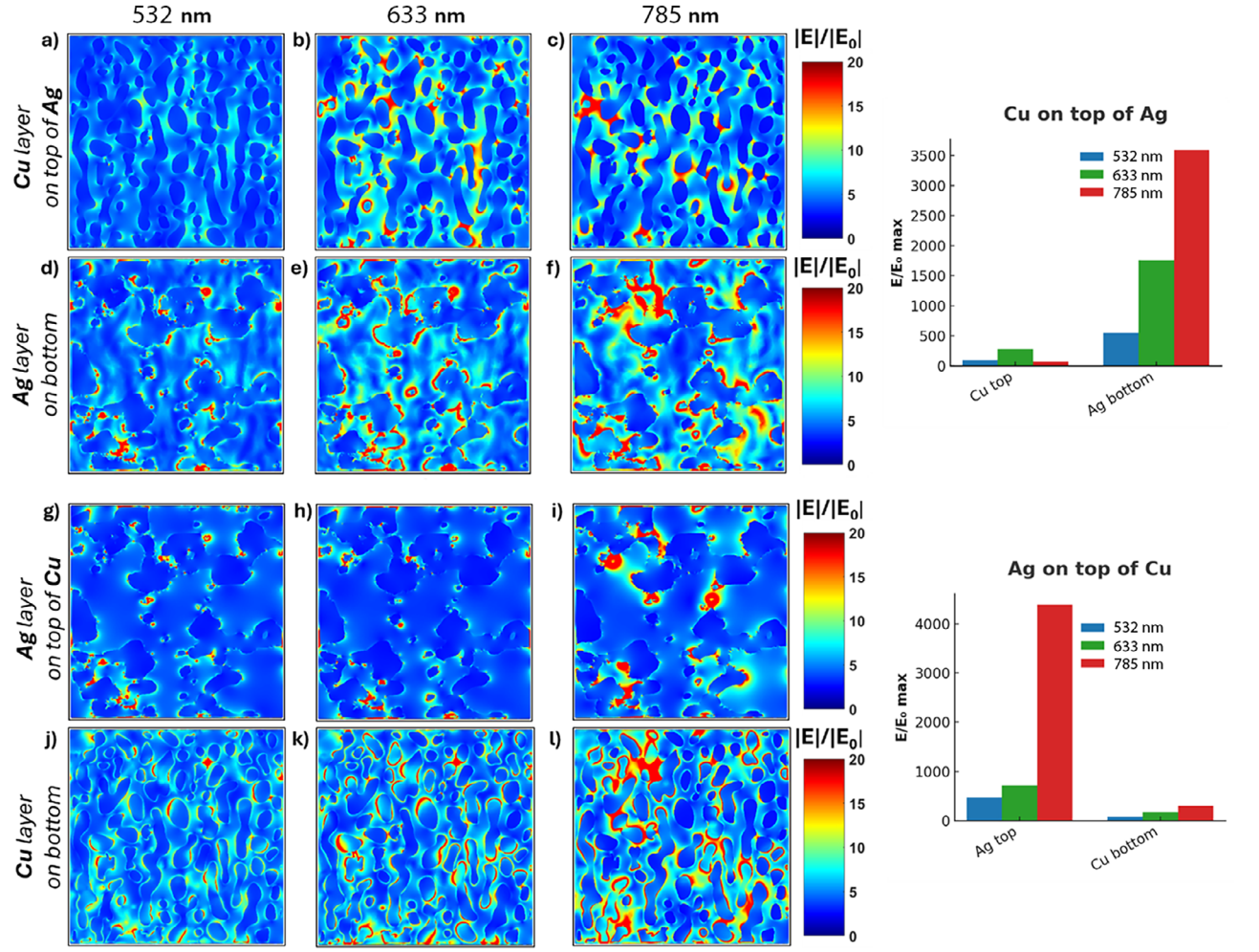

FIGURE 5 | The enhanced EM field distribution of Ag and Cu layers for(a–f) Ag/Cu and (g–l) Cu/Ag NPMs calculated as a ratio of the electric field in the presence of nanoporous metals to the incident field for different wavelengths.

configurations are shown in Figure 6d–f. Detailed vibrational assignments for these characteristic peaks are provided in Table S2.To account for possible peak shifts, each intensity was extracted as the maximum value within a ±10 cm^{-1} window centered on the nominal Raman shift.

Under 532 nm excitation, the averaged spectra of 0.1 μM R6G in Figure 6a show that both bilayer Ag/Ag and Ag/Cu configurations exhibit relatively stronger enhancement, homometallic Au/Au ranked next, while Cu/Cu is the worst. This trend is highly consistent with our numerical simulations in Figures 2–5, which predicted Ag-based configurations dominate the EM field enhancement due to its superior plasmonic properties, Cu/Cu exhibits negligible plasmonic activity. A quantitative comparison of the five characteristic band intensities (Figure 6d) reveals that these two configurations perform almost similarly, with Ag/Cu yielding slightly higher values for most bands, although the differences are marginal given that each intensity was extracted as the maximum within a ±10 cm^{-1} window. Based on this analysis, Ag/Cu was selected for our further limit of detection (LOD) studies. To understand the mechanism behind the strong performance of Ag/Cu at 532 nm, we also examine both numerical simulations and ellipsometric data. The FEM simulations in Figure 5a–f show that although the top Cu exhibits negligible plasmonic activity, the bottom Ag still supports strong field localization, indicating that incident light partially penetrates the Cu layer and excites the buried Ag. This interpretation is further supported by ellipsometric data (Figure S8g and Table S1). At 532 nm (2.33 eV), the Ag/Cu NPMs exhibits a weakly negative real permittivity (ε′) and moderate absorption (ε′′). This "loss-balanced" dielectric response allows efficient excitation of the buried Ag while preventing excessive radiative damping, resulting in the strong enhancement observed experimentally.

As shown in Figure 6b, under 633 nm excitation with 1 μM R6G, the homometallic bilayer Ag/Ag NPMs clearly outperforms the Au/Au nanoporous structure, while the bilayer Cu/Ag and other configurations show comparatively weaker enhancements. Again, the homometallic Cu/Cu NPMs exhibits the poorest performance same as under 532 nm excitation above. This trend is corroborated by the extracted intensities of the five characteristic Raman bands shown in Figure 6e, which reveal that the homometallic Ag/Ag substrates produces signals approximately 2.5 times stronger than those obtained from the homometallic Au/Au NPMs.

This result is fully consistent with our numerical simulations (Figures 2–5), which predict that Ag/Ag exhibits its strongest

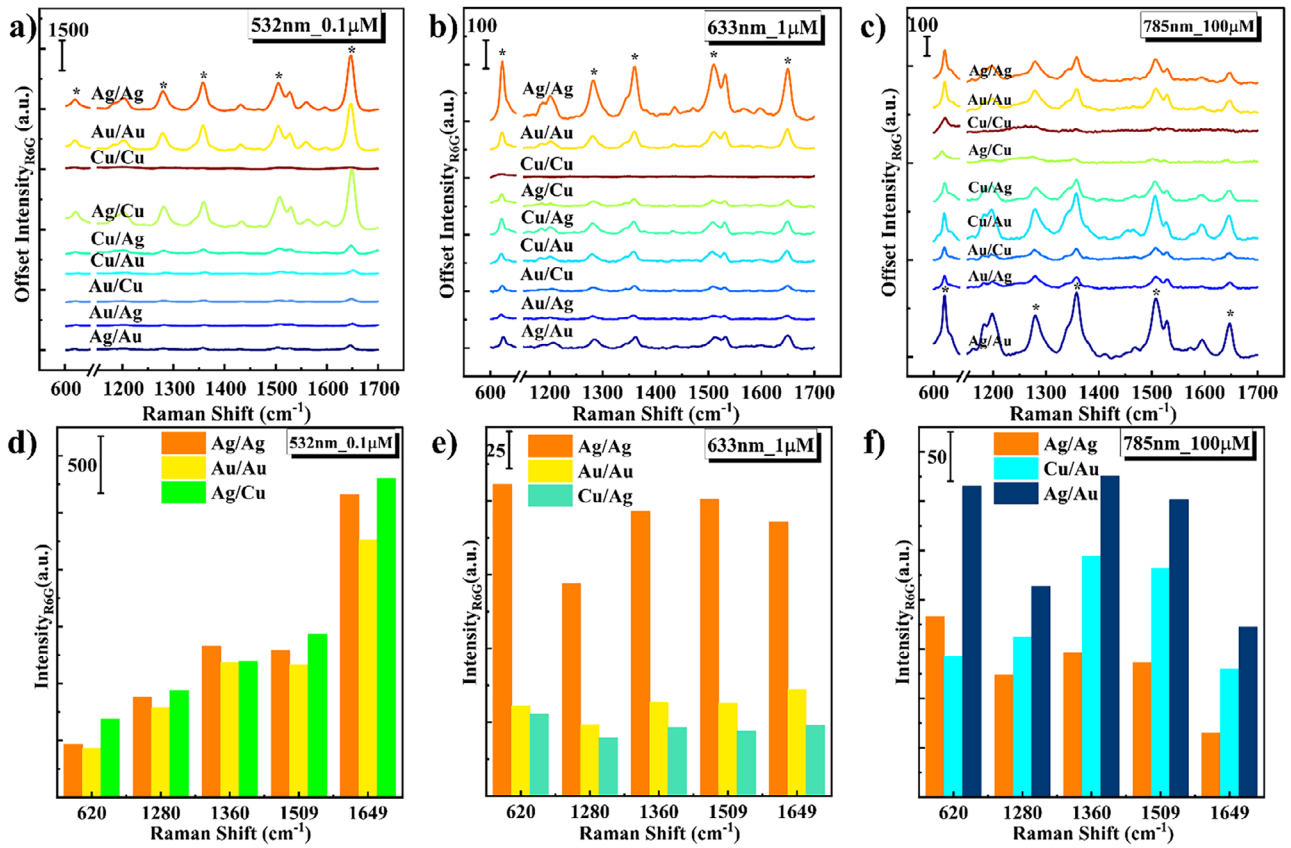

FIGURE 6 | SERS spectra of R6G on various substrates under excitation wavelengths of (a) 532 nm, (b) 633 nm and (c) 785 nm; (d–f): Comparison of the five characteristic R6G band intensities for the top three NPMs configurations identified in Figure 6a–c, respectively.

EM field enhancement precisely at 633 nm, outperforming all other configurations at this excitation wavelength. The physical mechanism behind this superior performance can be understood from the dielectric properties of silver: as shown in Figure S8a and Table S1, Ag/Ag exhibits a strongly negative real permittivity (ε') across the visible range with minimal optical losses, enabling efficient plasmon excitation and strong near-field confinement. At 633 nm, this optimal dielectric response coincides with the intrinsic plasmon resonance of nanostructured silver, leading to maximum field enhancement. In contrast, Au/Au shows broader dispersion and higher losses (Figure S9d), while Cu-based configurations exhibit negligible plasmonic activity due to their weak negative ε' and strong absorption (Figure S9g).

Under 785 nm excitation with 100 μM R6G shown in Figure 6c, a distinct trend is observed: the Ag/Au configuration performs the strongest R6G signal enhancement, followed by Cu/Au and homometallic Ag/Ag. It is worth noting that this experimental ranking differs partially from our numerical simulations (Figures 2–5), which predict that at 785 nm, Cu/Ag should rank among the top performers, while Ag/Cu and Ag/Ag show comparable enhancement, while Ag/Au exhibit moderate activity. Specifically, the simulations indicate stronger activity for Cu/Ag than observed experimentally, whereas Ag/Au and Cu/Au appear more prominent in our measurements. We attribute these discrepancies to oxidation effect. The SERS measurements presented in Figure 6 were performed on multiple batches of samples under three visible laser wavelengths, and due to the sequential nature of the experiments, some substrates might measure after a longer storage period (exceeding one month) following fabrication. During this time, the exposed Ag layers in configurations such as Cu/Ag and Ag/Cu likely underwent oxidation, leading to signal degradation. In contrast, the Ag/Au and Cu/Au configurations benefit from a protective Au top layer that shields the bottom Ag from oxidation, preserving their plasmonic activity. To test this hypothesis, additional measurements were performed on NPMs within two weeks of fabrication, as presented in Supporting Information. The SERS performance of different bilayer NPMs (Ag/Ag, Ag/Au, Ag/Cu) was re-evaluated under 785 nm excitation (Figure S1). A direct comparison reveals that the homometallic Ag/Ag NPM exhibits the highest enhancement capability, successfully detecting R6G at a concentration of 0.1 μM, whereas under identical conditions, the bilayer Ag/Au and Ag/Cu NPMs only yielded measurable signals at a higher concentration of 1 μM. This result clearly confirms that the homometallic bilayer Ag/Ag NPM offers superior intrinsic SERS sensitivity at 785 nm excitation, in full agreement with the simulation results presented in Figures 2–5.

Further evidence comes from aging studies over a two-month storage period (Figures S2–S4). After storage, the Ag/Ag bilayer—which initially showed strong enhancement—exhibited significant signal degradation under all excitation wavelengths, while configurations with a protective Au top layer (Ag/Au, Cu/Au, Au/Ag) maintained their activity much better. For instance, under 785 nm excitation (Figure S4), Ag/Au and Cu/Au consistently outperformed other configurations after storage, despite being only moderate performers in fresh measurements. These

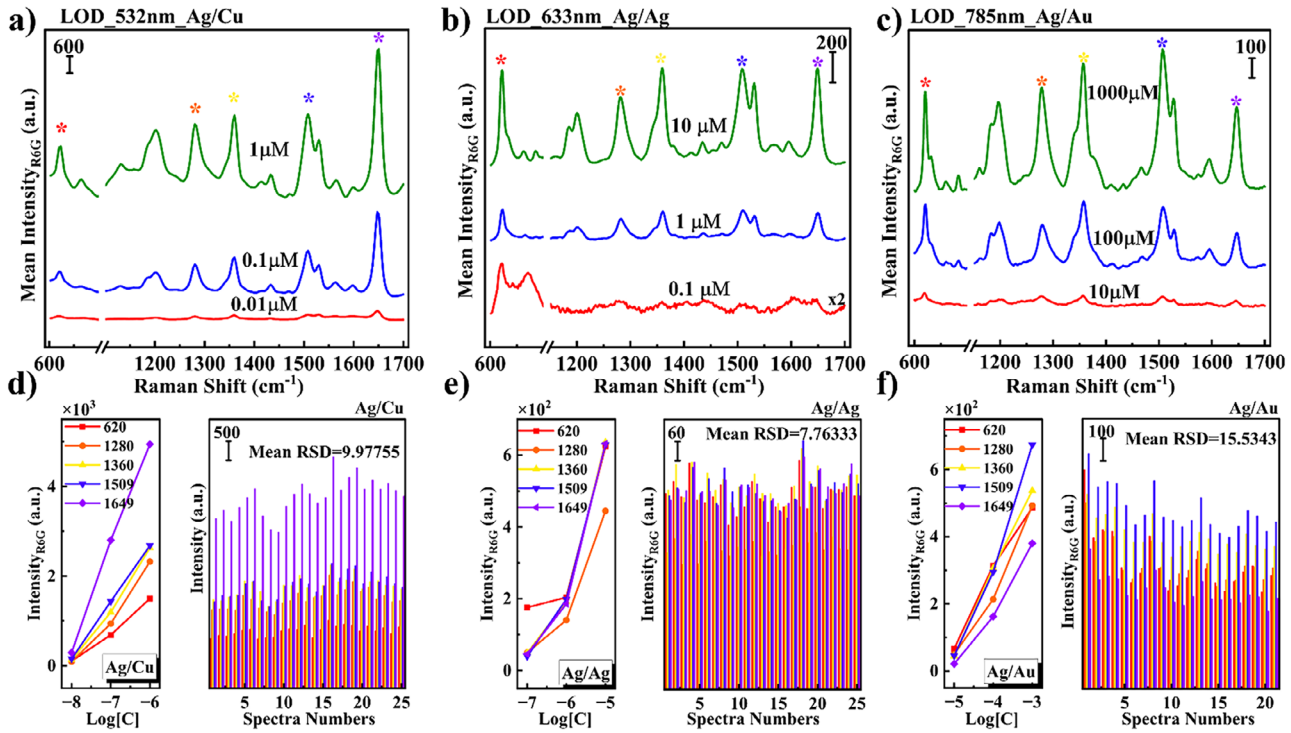

FIGURE 7 | (a–c) Concentration-dependent SERS spectra of R6G on Ag/Cu, Ag/Ag and Ag/Au NPMs under 532, 633 and 785 nm, respectively. (d–f) Left panels: Calibration curves for the five characteristic bands (620, 1280, 1360, 1509, and 1649 cm^{-1}) derived from the corresponding SERS spectra shown in (a–c); Right panels: Intensity distribution of these bands from randomly selected spectra for 1 μM, 10 μM and 1 mM R6G on the respective substrates.

observations confirm that while Ag/Ag possesses the highest intrinsic plasmonic activity, its susceptibility to oxidation limits its long-term stability. In contrast, Au-protected configurations offer a valuable trade-off between enhancement efficiency and durability, making them particularly attractive for practical applications where sample storage and handling are unavoidable.

To further evaluate SERS performance, we examined signal uniformity, limit of detection (LOD), and concentration dependence of the best-performing bilayer configurations identified above for excitation wavelengths of 532, 633, and 785 nm. Accordingly, bilayer Ag/Cu, homometallic Ag/Ag, and Ag/Au NPMs were investigated using 532, 633, and 785 nm excitation, respectively. The results are presented in Figure 7. Figure 7a–c show the averaged SERS spectra of R6G at different concentrations, all acquired under consistent experimental conditions. The lowest detectable concentrations of R6G were determined to be as low as 0.01, 0.1, and 10 μM for 532, 633, and 785 nm excitation wavelengths, respectively. Concentration calibration curves are shown in Figure 7d–f left panels, derived from the five characteristic SERS bands at 620, 1280, 1360, 1509, and 1649 cm^{-1} in the averaged SERS spectra shown in Figure 7a–c. We found that the intensities of five characteristic SERS bands of R6G exhibit an essentially linear relationship with the logarithm of the corresponding R6G concentrations, which is consistent with the results in the literature [42].

The right panels of Figure 7d–f show the intensity distributions of five selected SERS bands obtained from multiple randomly collected spectra across different NPM configurations. For each characteristic R6G peak, the relative standard deviation (RSD) of the intensities was calculated, followed by averaging the RSD values over the five peaks. This resulted in mean RSDs of 9.98%, 7.76%, and 15.53% for the Ag/Cu, Ag/Ag, and Ag/Au bilayer NPMs, respectively, indicating high reproducibility and uniformity of the SERS response across the nanoporous substrates.

In addition, complementary experiments were carried out on tri-layer NPMs to investigate the influence of layer sequence on SERS performance. As illustrated in Figure S6, all the three layers configurations exhibited concentration-dependent SERS enhancement for R6G under 532, 633, and 785 nm excitation, with the Ag/Au/Cu structure delivering the strongest signal intensity. However, the overall performance of the tri-layer structures remained inferior to that achieved with the bilayer configurations discussed here.Detailed spectra and peak assignments are provided in the (Figure S6).

The translation of SERS substrates from conceptual fabrication to practical application is a critical step in biosensing, particularly for the early screening and diagnosis of cancers and related biomarkers [43–45]. The ability to detect low-concentration biomarkers with high specificity and sensitivity provides a crucial, time-sensitive advantage for early diagnosis and subsequent therapeutic intervention. In a recent work, we identified ADAMTS3 as a novel mechanistic serum biomarker for hepatocellular carcinoma (HCC) and reported its characteristic

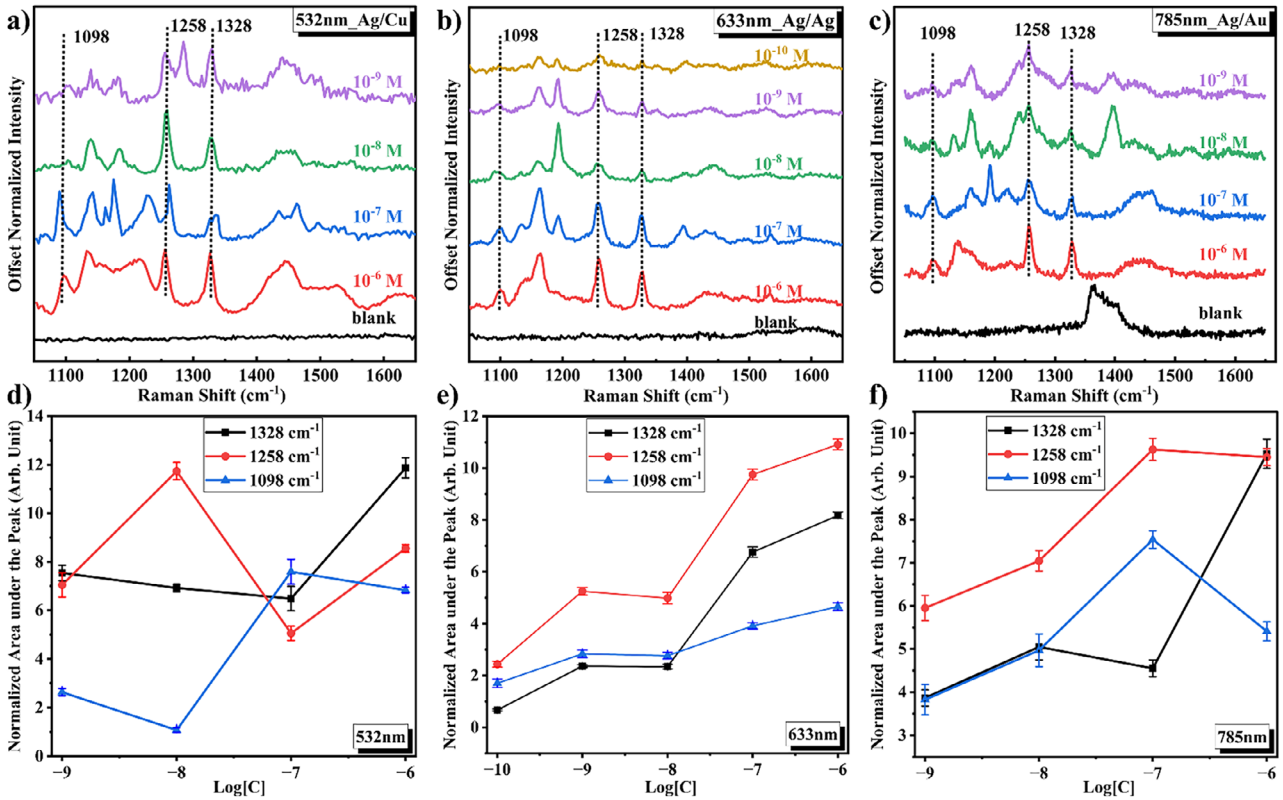

FIGURE 8 | (a–c) Normalized SERS spectra of ADAMTS3 at various concentrations on Ag/Cu, Ag/Ag, and Ag/Au NPMs under 532, 633, and 785 nm excitation, respectively. (d–f) Fit-integrated areas under the corresponding characteristics bands marked with dot lines in (a–c).

SERS fingerprint [46]. Three distinct Raman peaks at 1097cm^{-1}, 1258cm^{-1}, and 1328 cm^{-1} were observed in that study. Based on established Raman assignments for proteins and nucleic acids [47–50], these peaks can be attributed the band at 1097 cm^{-1} corresponds to O—P—O^{-} stretching vibrations of the phosphate backbone, which may originate from either the DNA aptamer or phosphorylated residues in ADAMTS3; the peak at 1258 cm^{-1} falls within the characteristic amide III region (1200–1350 cm^{-1}) and reflects C—N stretching coupled with N—H bending, sensitive to protein secondary structure (specifically random coil or β-sheet conformations); and the band at 1328 cm^{-1} is assigned to the amide III band of α-helical structures in the protein backbone. These spectral features provide a unique molecular signature for ADAMTS3 detection. In that study, we developed a DNA origami-based SERS platform that enabled sensitive detection of ADAMTS3 at concentrations as low as 10^{-10}M. These spectral features provide a unique molecular signature for ADAMTS3 detection [46]. Here, we build upon our previous findings by deploying the novel bi-layer metal NPMs as a superior SERS substrate to re-investigate the detection of the same ADAMTS3 protein. As discussed above, these substrates offer large, uniform active area and long-term stability, therefore they can be interesting for applied SERS biosensing.

Figure 8 presents the analytical performance of the bi-layer NPMs for the detection of ADAMTS3 under visible excitation. Specifically, Figure 8a–c displays the normalized mean SERS spectra of ADAMTS3 protein at various concentrations, acquired using 532, 633, and 785 nm laser excitation wavelengths, respectively. Each set of spectra corresponds to the optimally designed bi-layer configuration (e.g. Ag/Cu, homometallic Ag/Ag, and Ag/Au) for the respective laser wavelength, as detailed in the previous sections. The fitted areas under the characteristic SERS bands of ADAMTS3 protein (marked by dotted lines in a–c) at 1098, 1258, and 1328 cm^{-1} were plotted in Figure 8d–f as a function of logarithmic concentration with error bars. The peak fitting was performed using a Gaussian function, consistent with our previous methodology [51]. It should be noted that several peaks in the 1150–1200 cm^{-1} region were observed in the SERS spectra (Figure 8). However, these peaks showed no consistent correlation with ADAMTS3 concentration and exhibited irregular intensity variations across different measurements. As their origin could not be definitively assigned, they were excluded from the quantitative fitting analysis to ensure the reliability of the concentration-dependent results.

As shown in Figure 8a–c, the characteristic SERS peaks of the ADAMTS3 protein remain clearly identifiable at a concentration of 10^{-9} M when using the three optimal enhancement substrates—Ag/Cu, Ag/Ag, and Ag/Au—under 532, 633, and 785 nm excitation, respectively. Notably, under 633 nm excitation wavelength, these characteristic peaks are still detectable at a lower concentration of 10^{-10} M, demonstrating an enhancement factor comparable to that reported in our recent work employing a well-established structure high-sensitivity SERS platform, namely Au-dimer/DNA origami structures [46, 52, 53]. Moreover, the fitted areas of the characteristic peaks at 1098, 1258, and 1328 cm^{-1} were plotted as a function

of the logarithmic concentration. For 633 nm excitation, the data exhibit smaller error bars relative to those obtained at 532 and 785 nm, and follow an approximately linear trend. This suggests that the peak areas increase nearly linearly with protein concentration, in agreement which our previous findings [46].

In contrast, such a linear relationship is not consistently observed under 532 and 785 nm excitation. At 785 nm, the fitted peak areas at 1098 and 1258 cm^{-1} display an approximately linear trend over the concentration range of 10^{-7} to 10^{-9} M; however, a clear deviation occurs at 10^{-6} M, and all data points are associated with relatively large error bars. Under 532 nm excitation, the dependence of fitted peak area on logarithmic concentration deviates entirely from linearity for all three characteristic peaks, accompanied by significantly larger uncertainties compared to the other wavelengths.

This pronounced nonlinearity and increased data scatter can be attributed to wavelength-dependent electronic interactions Between the protein and the bimetallic substrate. As discussed in the Introduction, the adsorption behavior of molecules containing polar or partially charged groups—such as those in the ADAMTS3 protein—is highly sensitive to the electronic structure of the metals surface. We therefore hypothesize that, Under 532 nm excitation, the specific bilayer configuration (e.g., Ag/Cu) exhibits an electronic environment that promotes non-uniform or partially saturable protein adsorption Across the concentration range. This leads to inconsistent SERS responses, greater variability in measured intensities, and consequently, a breakdown of linearity With increased experimental uncertainty

4 | Conclusions

In summary, we present a comprehensive study of stable, large-area, and cost-effective plasmonic platforms composed of stacked layers of noble plasmonic metals (NPMs). By fabricating a range of bilayer configurations (Au/Ag, Ag/Au, Au/Cu, Cu/Au, Ag/Cu, and Cu/Ag), we systematically investigated the influence of metal selection and stacking sequence on metal–metal interactions. Extensive numerical simulations, performed using both finite element methods (FEM, COMSOL) and fully atomistic modeling approaches, yielded detailed insights into the optical responses of these nanostructures under visible-range excitation at different energies. These complementary modeling techniques effectively capture the behavior of porous architectures, underscoring their potential not only for enhanced spectroscopic applications but also for broader functional uses.

Experimental validation was achieved through SERS measurements using both a standard molecular probe (R6G) and a biologically relevant target (the ADAMTS3 biomarker). The results confirm the strong performance of the bilayer platforms as SERS substrates and provide initial evidence that bimetallic architectures can promote interlayer coupling at the metal–metal interface. Overall, this work represents a promising step toward the development of complex, multimaterial plasmonic platforms for SERS, combining reproducibility, structural simplicity, and low fabrication cost.

Author Contributions

Y.Z. performed the Raman experiments and analyzed the data, A.S. and T.G. performed the numerical simulations, S.M. performed the XRD analyses, A.S., A.A., L.B., N.M. and I.M. supported the numerical simulations and results discussion, C.W. and H.J. supported the experimental measurements, A.D., G.L., S.W. and R.K. supported the samples fabrication, Z.J., Z.Z., and D.G. supervised the work. Y.Z. and A.S. equally contributed to the present work. All authors contributed to the writing of the manuscript.

Acknowledgements

The authors thank the National Natural Science Foundation of China (No.22202167), National Natural Science Foundation of China (62305092), the National Key Research and Development Project of China (No. 2023YFF0613603), Sichuan Science and Technology Program (2025YFHZ0333) and the HORIZON-MSCADN-2022: DYNAMO, grant Agreement 101072818. NM and BJ acknowledge the 'Excellence by Choice' Programme at Umeà University funded by Kempestielserna (Grant Number. JCK-2130.3). The authors thank the Clean Room Facility of IIT.

Open access publishing facilitated by Istituto Italiano di Tecnologia, as part of the Wiley - CRUI-CARE agreement.

Conflicts of Interest

The authors declare no conflict of interest.

Data Availability Statement

The data that support the findings of this study are available from the corresponding author upon reasonable request.

References

1. O. Guselnikova, A. Trelin, Y. Kang, et al., "Pretreatment-Free SERS Sensing of Microplastics Using a Self-Attention-Based Neural Network on Hierarchically Porous Ag Foams," *Nature Communications* 15, no. 1 (2024): 4351, https://doi.org/10.1038/s41467-024-48148-w.

2. Y. Jin, Z. Hu, H. Xu, et al., "Bioinspired Turing-Nanoarchitected Needle for Solid Matrices Analysis: a Universal Platform Enabling Dual-Scale SERS Enhancement," *Advanced Materials* 37 (2025): 2506426, https://doi.org/10.1002/adma.202506426.

3. T. Fujita, P. Guan, K. McKenna, et al., "Atomic Origins of the High Catalytic Activity of Nanoporous Gold," *Nature Materials* 11, no. 9 (2012): 775–780, https://doi.org/10.1038/nmat3391.

4. B. Zugic, L. Wang, C. Heine, et al., "Dynamic Restructuring Drives Catalytic Activity on Nanoporous Gold–Silver Alloy Catalysts," *Nature Materials* 16, no. 5 (2017): 558–564, https://doi.org/10.1038/nmat4824.

5. J. Fu, S. S. Welborn, and E. Detsi, "Dealloyed Air- and Water-Sensitive Nanoporous Metals and Metalloids for Emerging Energy Applications," *ACS Applied Energy Materials* 5, no. 6 (2022): 6516–6544, https://doi.org/10.1021/acsaem.2c00405.

6. A. N. Koya, X. Zhu, N. Ohannesian, et al., "Nanoporous Metals: from Plasmonic Properties to Applications in Enhanced Spectroscopy and Photocatalysis," *ACS Nano* 15, no. 4 (2021): 6038–6060, https://doi.org/10.1021/acsnano.0c10945.

7. J. Singh, A. Chopra, S. S. Pal, and S. Sarkar, "Nanoporous Gold Films as a Perfect NIR–UV Absorber," *Applied Surface Science* 685 (2025): 162005, https://doi.org/10.1016/j.apsusc.2024.162005.

8. S. Rout, Z. Qi, M. M. Biener, et al., "Nanoporous Gold Nanoleaf as Tunable Metamaterial," *Scientific Reports* 11, no. 1 (2021): 1795, https://doi.org/10.1038/s41598-021-81128-4.

9. T. Tapani, J. M. Pettersson, N. Henriksson, et al., "Morphology-Modified Contributions of Electronic Transitions to the Optical Response of Plasmonic Nanoporous Gold Metamaterial," *Nature Communications* 17, no. 1 (2026): 829, https://doi.org/10.1038/s41467-026-68506-0.

10. S. Xiao, S. Wang, X. Wang, and P. Xu, "Nanoporous Gold: A Review and Potentials in Biotechnological and Biomedical Applications," *Nano Select* 2, no. 8 (2021): 1437–1458, https://doi.org/10.1002/nano.202000291.

11. R. Ron, E. Haleva, and A. Salomon, "Nanoporous Metallic Networks: Fabrication, Optical Properties, and Applications," *Advanced Materials* 30, no. 41 (2018): 1706755, https://doi.org/10.1002/adma.201706755.

12. G. Ruffato, D. Garoli, S. Cattarin, et al., "Patterned Nanoporous-Gold Thin Layers: Structure Control and Tailoring of Plasmonic Properties," *Microporous and Mesoporous Materials* 163 (2012): 153–159, https://doi.org/10.1016/j.micromeso.2012.07.027.

13. E. Detsi, M. Van De Schootbrugge, S. Punzhin, P. R. Onck, and J. T. M. De Hosson, "On Tuning the Morphology of Nanoporous Gold," *Scripta Materialia* 64, no. 4 (2011): 319–322, https://doi.org/10.1016/j.scriptamat.2010.10.023.

14. S. Mooraj, S. S. Welborn, S. Jiang, et al., "Three-Dimensional Hierarchical Nanoporous Copper via Direct Ink Writing and Dealloying," *Scripta Materialia* 177 (2020): 146–150, https://doi.org/10.1016/j.scriptamat.2019.10.013.

15. Y. Sun, Y. Ren, and K. Yang, "New Preparation Method of Micron Porous Copper Through Physical Vacuum Dealloying of Cu–Zn Alloys," *Materials Letters* 165 (2016): 1–4, https://doi.org/10.1016/j.matlet.2015.11.102.

16. E. Detsi, Z. Vuković, S. Punzhin, P. M. Bronsveld, P. R. Onck, and J. T. M. De Hosson, "Fine-Tuning the Feature Size of Nanoporous Silver," *CrystEngComm* 14, no. 17 (2012): 5402–5406, https://doi.org/10.1039/c2ce25313e.

17. E. Detsi, M. S. Sellès, P. R. Onck, and J. T. M. De Hosson, "Nanoporous Silver as Electrochemical Actuator," *Scripta Materialia* 69, no. 2 (2013): 195–198, https://doi.org/10.1016/j.scriptamat.2013.04.003.

18. P. Ponzellini, G. Giovannini, S. Cattarin, et al., "Metallic Nanoporous Aluminum–Magnesium Alloy for UV-Enhanced Spectroscopy," *The Journal of Physical Chemistry C* 123, no. 33 (2019): 20287–20296, https://doi.org/10.1021/acs.jpcc.9b04230.

19. D. Garoli, A. Schirato, G. Giovannini, et al., "Galvanic Replacement Reaction as a Route to Prepare Nanoporous Aluminum for UV Plasmonics," *Nanomaterials* 10, no. 1 (2020): 102, https://doi.org/10.3390/nano10010102.

20. T. Lee, H. Koh, A. K. Ng, J. Liu, E. A. Stach, and E. Detsi, "Ultrafine Nanoporous Aluminum by Electrolytic Dealloying of Aluminum-Magnesium Alloys in Glyme-Based Electrolytes With Recovery of Sacrificial Magnesium," *Scripta Materialia* 221 (2022): 114959, https://doi.org/10.1016/j.scriptamat.2022.114959.

21. D. Wang and P. Schaaf, "Plasmonic Nanosponges," *Advances in Physics: X* 3, no. 1 (2018): 1456361, https://doi.org/10.1080/23746149.2018.1456361.

22. Z. Wang, R. Liu, Z. Feng, et al., "Hierarchical Growth and Morphological Control of Ordered Cu–Au Alloy Arrays With High Surface Enhanced Raman Scattering Activity," *CrystEngComm* 22, no. 1 (2020): 113–118, https://doi.org/10.1039/C9CE01434A.

23. K. S. B. De Silva, V. J. Keast, and M. B. Cortie, "Effect of Al Additions on the Optical Properties of Au α-Phase," *Journal of Alloys and Compounds* 679 (2016): 225–230, https://doi.org/10.1016/j.jallcom.2016.04.054.

24. J. A. La, H. Lee, D. Kim, H. Ko, and T. Kang, "Enhanced Molecular Interaction of 3D Plasmonic Nanoporous Gold Alloys by Electronic Modulation for Sensitive Molecular Detection," *Nano Letters* 24, no. 23 (2024): 7025–7032, https://doi.org/10.1021/acs.nanolett.4c01505.

25. X. T. Van, L. T. Trinh, H. Van Pham, and M. T. T. Nguyen, "Tunable Plasmonic Properties of Bimetallic Au-Cu Nanorods for SERS-Based Sensing Application," *Journal of Electronic Materials* 51, no. 4 (2022): 1857–1865, https://doi.org/10.1007/s11664-022-09455-4.

26. S. Kaja and A. Nag, "Bimetallic Ag–Cu Alloy Microflowers as SERS Substrates With Single-Molecule Detection Limit," *Langmuir* 37, no. 44 (2021): 13027–13037, https://doi.org/10.1021/acs.langmuir.1c02119.

27. J. Liao, Y. Zhan, Q. Liu, et al., "Tunable Surface Plasmon Resonance of Al-Cu Bimetallic Nanoparticles Thin Films Induced by Pulsed-Laser," *Applied Surface Science* 540 (2021): 148397, https://doi.org/10.1016/j.apsusc.2020.148397.

28. G. M. Das, R. V. William, V. R. Dantham, and R. Laha, "Study on SERS Activity of Au-Ag Bimetallic Nanostructures Synthesized Using Different Reducing Agents," *Physica E: Low-dimensional Systems and Nanostructures* 129 (2021): 114656, https://doi.org/10.1016/j.physe.2021.114656.

29. M. Pisarek, M. Krawczyk, M. Hołdyński, et al., "Hybrid Nanostructures Based on TiO_2 Nanotubes With Ag, Au, or Bimetallic Au–Ag Deposits for Surface-Enhanced Raman Scattering (SERS) Applications," *The Journal of Physical Chemistry C* 127, no. 50 (2023): 24200–24210, https://doi.org/10.1021/acs.jpcc.3c04147.

30. J. E. S. Van Der Hoeven, T.-S. Deng, W. Albrecht, et al., "Structural Control Over Bimetallic Core–Shell Nanorods for Surface-Enhanced Raman Spectroscopy," *ACS Omega* 6, no. 10 (2021): 7034–7046, https://doi.org/10.1021/acsomega.0c06321.

31. H. Kwon, H.-N. Barad, A. R. Silva Olaya, et al., "Dry Synthesis of Pure and Ultrathin Nanoporous Metallic Films," *ACS Applied Materials & Interfaces* 15, no. 4 (2023): 5620–5627, https://doi.org/10.1021/acsami.2c19584.

32. T. Tapani, V. Caligiuri, Y. Zou, et al., "Disordered Plasmonic System With Dense Copper Nano-Island Morphology," *Nanophotonics* 14, no. 12 (2025): 2151–2160, https://doi.org/10.1515/nanoph-2024-0743.

33. V. Caligiuri, H. Kwon, A. Griesi, et al., "Dry Synthesis of Bi-Layer Nanoporous Metal Films as Plasmonic Metamaterial," *Nanophotonics* 13, no. 7 (2024): 1159–1167, https://doi.org/10.1515/nanoph-2023-0942.

34. A. Hubarevich, J.-A. Huang, G. Giovannini, et al., "λ-DNA Through Porous Materials—Surface-Enhanced Raman Scattering in a Simple Plasmonic Nanopore," *The Journal of Physical Chemistry C* 124, no. 41 (2020): 22663–22670, https://doi.org/10.1021/acs.jpcc.0c06165.

35. L. Bonatti, G. Gil, T. Giovannini, S. Corni, and C. Cappelli, "Plasmonic Resonances of Metal Nanoparticles: Atomistic vs. Continuum Approaches," *Frontiers in chemistry* 8 (2020): 340, https://doi.org/10.3389/fchem.2020.00340.

36. T. Giovannini, L. Bonatti, P. Lafiosca, et al., "Do We Really Need Quantum Mechanics to Describe Plasmonic Properties of Metal Nanostructures?," *ACS Photonics* 9, no. 9 (2022): 3025–3034, https://doi.org/10.1021/acsphotonics.2c00761.

37. T. Giovannini, M. Rosa, S. Corni, and C. Cappelli, "A Classical Picture of Subnanometer Junctions: An Atomistic Drude Approach to Nanoplasmonics," *Nanoscale* 11, no. 13 (2019): 6004–6015, https://doi.org/10.1039/C8NR09134J.

38. P. Lafiosca, T. Giovannini, M. Benzi, and C. Cappelli, "Going Beyond the Limits of Classical Atomistic Modeling of Plasmonic Nanostructures," *The Journal of Physical Chemistry C* 125, no. 43 (2021): 23848–23863, https://doi.org/10.1021/acs.jpcc.1c04716.

39. S. Zanotto, L. Bonatti, M. F. Pantano, et al., "Strain-Induced Plasmon Confinement in Polycrystalline Graphene," *ACS Photonics* 10, no. 2 (2023): 394–400, https://doi.org/10.1021/acsphotonics.2c01157.

40. L. Nicoli, P. Lafiosca, P. Grobas Illobre, L. Bonatti, T. Giovannini, and C. Cappelli, "Fully Atomistic Modeling of Plasmonic Bimetallic Nanoparticles: Nanoalloys and Core-Shell Systems," *Frontiers in Photonics* 4 (2023): 1199598, https://doi.org/10.3389/fphot.2023.1199598.

41. T. Giovannini, P. G. Illobre, P. Lafiosca, et al., "plasmonX: An Open-Source Code for Nanoplasmonics," *Computer Physics Communications* 322 (2026): 110035, https://doi.org/10.1016/j.cpc.2026.110035.

42. Q. Xia, Y. Jia, C. Bi, et al., "Nanoporous Ag Microparticles With Tailorable and Noncontaminated Nanopores for SERS Sensing Applications," *Advanced Materials* 37, no. 13 (2025): 2414962, https://doi.org/10.1002/adma.202414962.

43. M. Blanco-Formoso and R. A. Alvarez-Puebla, "Cancer Diagnosis through SERS and Other Related Techniques," *International Journal of Molecular Sciences* 21, no. 6 (2020): 2253, https://doi.org/10.3390/ijms21062253.

44. H. Shin, B. H. Choi, O. Shim, et al., "Single Test-Based Diagnosis of Multiple Cancer Types Using Exosome-SERS-AI for Early Stage Cancers," *Nature Communications* 14, no. 1 (2023): 1644, https://doi.org/10.1038/s41467-023-37403-1.

45. L. Guerrini, N. Pazos-Perez, E. Garcia-Rico, and R. Alvarez-Puebla, "Cancer Characterization and Diagnosis With SERS-Encoded Particles," *Cancer Nanotechnology* 8, no. 1 (2017): 5, https://doi.org/10.1186/s12645-017-0031-3.

46. C. Wang, H. Jin, Q. Zhang, et al., "ADAMTS3 as a Promising Novel Biomarker for the Diagnosis of Hepatocellular Carcinoma," bioRxiv,Preprint (September 20, 2025), 2025–2109, https://doi.org/10.1101/2025.09.17.676767.

47. N.-T. Yu and S. Krimm, "Raman Spectroscopy: A Conformational Probe in Biochemistr," *CRC Critical Reviews in Biochemistry* 4, no. 3 (1977): 229–280, https://doi.org/10.3109/10409237709102559.

48. A. Rygula, K. Majzner, K. M. Marzec, A. Kaczor, M. Pilarczyk, and M. Baranska, "Raman Spectroscopy of Proteins: a Review," *Journal of Raman Spectroscopy* 44, no. 8 (2013): 1061–1076, https://doi.org/10.1002/jrs.4335.

49. N. Kuhar, S. Sil, T. Verma, and S. Umapathy, "Challenges in Application of Raman Spectroscopy to Biology and Materials," *RSC Advances* 8, no. 46 (2018): 25888–25908, https://doi.org/10.1039/C8RA04491K.

50. Z. Movasaghi, S. Rehman, and I. U. Rehman, "Raman Spectroscopy of Biological Tissues," *Applied Spectroscopy Reviews* 42, no. 5 (2007): 493–541, https://doi.org/10.1080/05704920701551530.

51. Y. Zou, L. Mattarozzi, H. Jin, et al., "UV-SERS Monitoring of Plasmonic Photodegradation of Biomolecules on Aluminum Platforms Decorated With Rhodium Nanoparticles," *Nanoscale Advances* 7, no. 17 (2025): 5212–5220, https://doi.org/10.1039/D5NA00486A.

52. Y. Zou, H. Jin, Q. Ma, et al., "Advances and Applications of Dynamic Surface-Enhanced Raman Spectroscopy (SERS) for Single Molecule Studies," *Nanoscale* 17 (2025): 3656–3670, https://doi.org/10.1039/D4NR04239E.

53. N. Maccaferri, G. Barbillon, A. N. Koya, G. Lu, G. P. Acuna, and D. Garoli, "Recent Advances in Plasmonic Nanocavities for Single-Molecule Spectroscopy," *Nanoscale Advances* 3, no. 3 (2021): 633–642, https://doi.org/10.1039/D0NA00715C.

Supporting Information

Additional supporting information can be found online in the Supporting Information section.

Supporting File: admi70543-sup-0001-SuppMat.docx.